

1 Growth of stylolite teeth patterns depending on normal stress and
2 finite compaction

3
4 *Koehn, Daniel; **Renard, François; ***Toussaint, Renaud; *Passchier, Cees W.

5
6 *Tectonophysics, Institute of Geosciences, University of Mainz, Becherweg 21, 55099
7 Mainz, Germany, email: koehn@uni-mainz.de

8 **LGIT-CNRS-Observatoire, Université Joseph Fourier BP 53, F-38041 Grenoble, France &
9 Physics of Geological Processes, University of Oslo, Norway

10 ***Institut de Physique du Globe de Strasbourg, UMR CNRS 7516, 5 rue Descartes, F-67084
11 Strasbourg Cedex, France

12
13
14 **Abstract**

15 Stylolites are spectacular rough dissolution surfaces that are found in many rock types.
16 They are formed during a slow irreversible deformation in sedimentary rocks and therefore
17 participate to the dissipation of tectonic stresses in the Earth's upper crust. Despite many
18 studies, their genesis is still debated, particularly the time scales of their formation and the
19 relationship between this time and their morphology.

20 We developed a new discrete simulation technique to explore the dynamic growth of
21 the stylolite roughness, starting from an initially flat dissolution surface. We demonstrate that
22 the typical steep stylolite teeth geometry can accurately be modelled and reproduce natural
23 patterns. The growth of the roughness takes place in two successive time regimes: i) an initial
24 non-linear increase in roughness amplitude that follows a power-law in time up to ii) a critical
25 time where the roughness amplitude saturates and stays constant. We also find two different
26 spatial scaling regimes. At small spatial scales, surface energy is dominant and the growth of
27 the roughness amplitude follows a power-law in time with an exponent of 0.5 and reaches an
28 early saturation. Conversely, at large spatial scales, elastic energy is dominant and the growth
29 follows a power-law in time with an exponent of 0.8. In this elastic regime, the roughness
30 does not saturate within the given simulation time.

31 Our findings show that a stylolite's roughness amplitude only captures a very small
32 part of the actual compaction that a rock experienced. Moreover the memory of the

33 compaction history may be lost once the roughness growth saturates. We also show that the
34 stylolite teeth geometry tracks the main compressive stress direction. If we rotate the external
35 main compressive stress direction, the teeth are always tracking the new direction. Finally, we
36 present a model that explains why teeth geometries form and grow non-linearly with time,
37 why they are relatively stable and why their geometry is strongly deterministic while their
38 location is random.

39 **1. Introduction**

40 Dynamic roughening of interfaces is an important research topic in many scientific
41 disciplines. A natural and spectacular example of such processes are stylolites, pairs of
42 dissolution surfaces facing each other, that are found in many rocks, mostly in limestones, and
43 which are often used for ornamental stone. A characteristic feature of stylolite interfaces is
44 their pronounced roughness with "teeth"- or "pen"-like geometries [stylus = pen, 1-5]. The
45 dark residual material that is collected within the stylolite consists mostly of clay particles [6].
46 Stylolites have mainly been described qualitatively in Earth Sciences so that dynamic models
47 of their growth and scaling properties are only now emerging [6-8]. However, the
48 development mechanism of their teeth-geometry, with peculiar square peaks (Fig. 1), is up to
49 now not understood.

50 Stylolites tend to grow perpendicular to the maximum compressive stress direction,
51 and exhibit a pronounced roughness on several scales [3]. Teeth like peaks develop with sides
52 oriented sub-parallel to the maximum stress direction (Fig. 1)[9]. The orientation of stylolites
53 and their teeth is commonly used by geologists as an indicator for the direction of the
54 maximum compressive stress [10-12] and the amplitude of the stylolite roughness is
55 sometimes used as a direct estimate of the compaction that the rock underwent [13]. We use
56 compaction here not only for a reduction in porosity of a rock but also for a vertical
57 shortening of the rock due to the weight of the overlying sediments. Studies on the validity of
58 these “rule of thumb” methods of compaction estimates are clearly missing, and the reason for

59 this is probably the complexity of the development of stylolites. Since stylolites are so
60 complex, there is also an ongoing debate in the literature about ways to classify them.

61 These features grow as a function of physical and chemical interactions and it is not
62 easy to study them experimentally [14] nor in numerical models [6]. However, experiments or
63 numerical models are needed since field observations alone cannot elucidate the dynamics of
64 the roughening process but only represent snapshots at a given time. Early works in Earth
65 Sciences classify stylolites according to their shape using qualitative methods [3]. However,
66 this classification cannot successfully encompass all stylolite patterns, which can be found in
67 numerous rock types and on a large range of scales [1-3]. Also, these classifications are often
68 not related to any specific material parameters, scaling properties or growth conditions. More
69 promising methods use qualitative descriptions of the stylolite roughness suggesting that they
70 are fractal surfaces [7,15] and self-affine structures [6,8,14]. Here we present new
71 microdynamic simulations of stylolite roughening that allow us to explore the dynamics of the
72 stress induced roughening process in time and space, illustrate stylolite geometries that
73 develop at different scales and propose a process-based explanation for the growth of stylolite
74 teeth. These simulations are based on first principles of physics and chemistry, without any ad
75 hoc phenomenological equation. It should also be underlined that contrarily to previous
76 linearized models [6,8], the model used here allows the exploration of the fully developed
77 structures, i.e. they take into account both, the non-linearities of the system that can be
78 associated to large departures from flat surfaces and the solid-solid contacts occurring through
79 the stylolite.

80 **2. The numerical model**

81 We start with an initially flat interface where dissolution can take place and the solid
82 can only dissolve and not precipitate. This would be the case with an undersaturated fluid
83 facing the solid. This flat interface may represent an initial “anticrack”, that is assumed to
84 represent the stylolite at an early stage of formation [16,17]. The model is two-dimensional

85 and it assumes that everything that dissolves along the interface is transported instantaneously
 86 in the fluid out of the system, i.e. that diffusion in the fluid pocket is not limiting the process,
 87 but happens at a much faster time scale than the dissolution itself. Accordingly, the fluid has a
 88 constant solute concentration. The model is part of the modelling environment "Elle" [18].
 89 The setup of the model is as follows: two solids are pressed together with a confined fluid
 90 layer in between them (Fig. 2). The right and left hand side of the model are fixed through
 91 elastic walls whereas the lower and upper walls of the model are moved inwards at a constant
 92 displacement rate. The solid is made up of small particles that are connected via linear elastic
 93 springs along a hexagonal lattice. These elements can represent either a single grain or a pack
 94 of smaller grains. At a scale larger than the grains, this network behaves in a classical
 95 elastostatic way.

96 *2.1 Thermodynamics and kinetics of stylolite dissolution*

97 Dissolution of the solid takes place in small steps dimensioned in such a way that one
 98 element of the solid is dissolved at every step. Dissolution follows a simple linear rate law

$$99 \quad D = kV \left[1 - \exp\left(-\frac{\{\Delta\psi + \Delta\sigma_n\}V}{RT}\right) \right], \quad (1)$$

100 where D is the dissolution velocity of the interface (m s^{-1}), k a dissolution kinetics rate
 101 constant ($\text{mol m}^{-2} \text{s}^{-1}$), V the molecular volume of the solid ($\text{m}^3 \text{mol}^{-1}$), R the universal gas
 102 constant ($\text{J mol}^{-1} \text{K}^{-1}$), T the temperature ($^{\circ}\text{K}$), $\Delta\psi$ (J m^{-3}) the changes in Helmholtz free
 103 energy of the solid during dissolution of a solid element, and $\Delta\sigma_n$ (Pa) the normal stress
 104 gradients along the interface [further details of the derivation are given in 19,20]. The
 105 Helmholtz free energy takes into account the variations in elastic and in surface energy.

106 Changes in surface energy are calculated from the curvature of the interface. The
 107 surface energy (E^s) per area unit around a single element located at the interface can be
 108 expressed as

109
$$E^s = \frac{\gamma}{\rho}, \quad (2)$$

110 where γ is the surface free energy and ρ is the local radius of curvature of the interface. The
 111 local curvature is determined using the two neighbours of each element along the interface.
 112 The sign of the curvature ρ is such that it is driving dissolution in the rate law when the solid
 113 is convex towards the fluid, and precipitation when it is concave. We perform an average
 114 across the interface using the local surface energies of elements and those of their neighbours
 115 (up to $n = 40$ in each direction) with the expression

116
$$E_i^{avs} = \frac{1}{C} \sum_{h=1}^n \left(\frac{1}{(2h+1)^2} \sum_{j=0}^{2h+1} E_{i+j-h}^s \right), \quad (3)$$

117 where E_i^{avs} is now the average surface energy for element i , E_i^s the local surface energy for
 118 element i , and E_{i+j-h}^s surface energies of neighbouring elements along the interface, and

119
$$C = \frac{\pi^2}{4} - \frac{17}{9} \approx 0.578512$$
 is a normalization factor that ensures that the average surface

120 energy on all sites is preserved in this averaging procedure. The local surface energies are
 121 divided by the sum of added elements and their maximum distance (divided by the initial
 122 radius of curvature of a particle). This averaging procedure amounts to consider a coarse-
 123 grained surface energy, at the scale of a few elements, and allows to avoid artefacts that could
 124 arise from the discreteness of the model. In this way, a singular local term E_i^s obtained at a
 125 corner of the interface is smoothed for E_i^{avs} over a neighbourhood of a few grains. This
 126 procedure is commonly used in computational physics to avoid discreteness artefacts [21,22].

127 The above expression is equivalently represented as a discrete convolution operation

128
$$E_i^{avs} = \sum_{-\infty < j < \infty} f_j E_{i+j}^s. \quad (4)$$

129 with a tent function shown on Fig. (2a),

130
$$f_j = \frac{1}{C} \sum_{k=|j|}^{\infty} \frac{1}{(2k+1)^2} \text{ for } j \neq 0, \text{ and } f_0 = f_1. \quad (5)$$

131 Keeping the terms up to $n = 40$ in this sum, i.e. all terms in the sum of Eq. (4) for $|j| < 40$, we
 132 are left with an error of only 2% in the tail of the weight function. The value of the
 133 normalization constant C is obtained by requiring that the average coarse grained surface
 134 energy is equal to the average local surface energy, i.e. it is set up by the condition that

135
$$\sum_{-\infty < j < \infty} f_j = 1. \quad (6)$$

136

137 *2.2 Mechanics*

138 The elastic energy and the normal stress at the interface are determined using a lattice
 139 spring model for the solid where elements are connected by linear elastic springs. We assume
 140 that the solid deforms only elastically without internal plastic deformation, except for the
 141 irreversible dissolution events happening at the modelled interface. Stresses in the solid are
 142 determined using an over-relaxation algorithm where elements of the model are moved until a
 143 new equilibrium configuration is found. The equilibrium configuration is defined by a given
 144 relaxation threshold. The net force (F_i) acting on an element i at position x_i is

145
$$F_i = \sum_{(j)} \kappa (|x_i - x_j| - l) v_{i,j} + f_p, \quad (7)$$

146 where the sum is over all neighbours j , κ is a spring constant, l is the equilibrium distance
 147 between elements i and j , $v_{i,j}$ is a unit vector pointing from j to i and f_p is an external force
 148 like the repulsion from a wall.

149 The elastic energy (E^{el}) is directly evaluated at a node i as

150
$$E^{el} = \frac{1}{4V} \sum_{(j)} \kappa (|x_i - x_j| - l)^2, \quad (8)$$

151 where $V = \sqrt{3}/2l^2$ is the volume of an elementary cell. It can also be determined from the
 152 strain tensor (u_{ik}) that is calculated from the lattice spring model with the expression [23]

153
$$E^{el} = \frac{1}{2} \lambda_1 \left(\sum_i u_{ii} \right)^2 + \lambda_2 \sum_{i,k} (u_{ik})^2, \quad (9)$$

154 where λ_1 and λ_2 are the Lamé constants. We use the Einstein convention with summation
 155 over repeated indices. Differences in elastic energy in equation (9) refer to differences
 156 between a stressed and a non-stressed element. The Lamé constants are set up by the spring
 157 constant, the lattice constant and the hexagonal lattice configuration, i.e. $\lambda_1 = \sqrt{3}\kappa/(2l)$ and
 158 $\lambda_2 = \sqrt{3}\kappa/(4l)$, or equivalently, the Young modulus is $K = \lambda_1 + 2\lambda_2 / 3 = 2\kappa/(\sqrt{3}l)$, and the
 159 Poisson ratio is $\nu = \lambda_1 / (2\lambda_1 + 2\lambda_2) = 1/3$ [24].

161 Finally the normal stress at the interface is determined from the repulsion of the two solids at
 162 the interface where the repulsion only contains normal components, assuming that a fluid film
 163 with no shear stress exists at the interface [25]. In order to calculate changes in normal stress
 164 along the interface we calculate an average of the normal stress across the whole interface and
 165 define differences in stress as the local normal stress minus the average normal stress.

166 The simulation flow is as follows:

- 167 - First the outer walls are moved in a given time step to stress the system.
- 168 - Once the upper and lower solids meet at the interface stress builds up. The rate law
 169 (eq. 1) is then used to calculate if elements can dissolve in the given time step. If not
 170 the system is stressed again until the first element can dissolve.
- 171 - Once elements dissolve they are removed one at a time and the stress is calculated
 172 again. The time that is used up by the dissolution of a single element is averaged to be
 173 the time it takes to dissolve that element completely divided by the system size
 174 (number of elements in the x-direction). Dissolution of elements proceeds until the
 175 given time is used up and another deformation step is applied. Using a desktop
 176 workstation, each simulation lasts between 10 and 30 days; the stress relaxation being
 177 the most time consuming part.

178 *2.3 Simulation parameters and disorder*

179 The parameters used in the simulation should mimic those of the natural example (fig. 1).
180 For our idealized model we use a rock mainly made up of calcite with a molecular volume of
181 0.00004 m³/mol, a Young's Modulus of 80 GPa, a Poisson's ratio of 0.33 (given by the
182 model configuration), a surface free energy of 0.27 J/m², a temperature of 300 K and a
183 dissolution rate constant of 0.0001 mol/(m²s) [8]. In addition, the displacement rate of the
184 upper and lower boundaries is fixed at a constant value corresponding to strain rates of
185 compaction between 10⁻¹⁰ and 10⁻¹² s⁻¹ (see fig. 2).

186 In order to introduce heterogeneities to the system a bimodal variation is set on the
187 dissolution rate constants of the elements. The heterogeneity in the system is set such that 5%
188 of all elements have a dissolution rate constant that is half the rate constant of the other
189 elements, i.e. they dissolve slower and pin the surface. The initial spatial distribution of the
190 rate constants is set using a pseudorandom routine resulting in a probability of 5% of particles
191 dissolving more slowly, picked independently for each site. Using this procedure, a spatial
192 heterogeneity, also called quenched noise, is introduced in the initial rock.

193

194 **3. Results**

195 *3.1 Simulated stylolites and comparison with natural data*

196 At first we compare a simulated stylolite directly with a natural example. Figure 3
197 shows a simulation of a roughening stylolite in a model that is 400 elements wide and that has
198 an absolute horizontal size of 40 cm. One element in the model then has a diameter of 1 mm
199 and may represent a single grain in a natural rock. We can compare the simulation with the
200 natural stylolite shown in figure 1, especially with the inset. The simulated stylolite has a
201 width that is about 2/3 of the width of the natural stylolite in the inset (see the hammer for the
202 scale).

203 The simulated stylolite develops in 8000 years at a compaction rate of $3 \times 10^{-12} \text{ s}^{-1}$ and
204 has compacted by 25.6 cm or 64% (original height of the simulated box was 40 cm). Both
205 simulated and natural stylolites are visually very similar. They both produce pronounced teeth
206 with smaller scale roughness in between and on top of the teeth. The height of the teeth (up to
207 about 8 cm) and their width are comparable in the natural and the simulated stylolite implying
208 that both have similar scaling properties. The grain size of the simulated example (1 mm) is
209 larger compared to natural rocks, mainly because we are limited by the calculation time of the
210 model.

211 *3.2 Initiation of the stylolite roughness by interface pinning along heterogeneities*

212 The stylolite roughness is initiated by elements that dissolve slower. If the model
213 contains no heterogeneity the interface will only become rough on the scale of single elements
214 and remain flat on the larger scale. This is because surface energies and elastic energies are
215 minimized when the surface is flat. Therefore, both of these energies will prevent the surface
216 to roughen and the stylolite to grow [8]. Once the system contains heterogeneity, slower
217 dissolving elements continuously pin the surface and thus make it rougher (Fig. 4).
218 Dissolution takes a longer time to destruct a roughness that is pinned by slower dissolving
219 elements than to flatten an interface with no variation. The roughness is not stable but very
220 dynamic in time since an increasing amount of more slowly dissolving elements are pinning
221 the interface while the solid progressively dissolves. However, the slower dissolving elements
222 themselves may dissolve as well if the roughness produces locally very high surface energies
223 due to a strong curvature of the interface or high elastic energies due to stress concentrations
224 or if two slower dissolving elements meet on opposing interfaces. Dissolution of pinning
225 elements will then reduce the roughness again.

226 An example of the development of the roughness in a simulation and the effects of
227 interface pinning is illustrated in figure 4. Figure 4a shows the initial random distribution of
228 slower dissolving elements (small dark spots). This heterogeneity is frozen into the system at

229 the beginning and does not change during a simulation (quenched noise). The interface where
230 the stylolite is initiated is shown as a black line. While the solid dissolves, pinning elements
231 are progressively being collected within the interface (small white spots, fig. 4b to d).

232 Two distinctively different patterns develop during the pinning of the interface. On
233 one hand, one or a couple of elements pin very locally and produce local spikes. On the other
234 hand, larger parts of the interface may be pinned between two elements that are further apart.
235 These second pattern generates the teeth geometries, typical of stylolites, with teeth having
236 various widths.

237 Figure 4e illustrates three different cases of pinning schematically. Single pinning
238 elements produce spikes whereas two pinning elements that pin from the same side produce
239 teeth. The structures grow fastest when elements pin from opposing sides. The interfaces in
240 figures 4c and 4d illustrate the teeth-forming processes presented in figure 4e: the interface is
241 made up of single pinning elements, larger teeth where groups of elements pin and steep
242 interfaces where elements pin from opposing sides. The surface structure changes when new
243 pinning elements are collected within the stylolite and when pinning elements are destructed.
244 The amplitude of the stylolite grows during these processes (from figure 4b to d) and the
245 wavelength of the interface is also evolving. Small wavelengths can grow very fast (figure 4c)
246 whereas the larger wavelengths need longer time to develop (figure 4d).

247 Figure 5 shows the evolution of the growing roughness of two stylolites through time
248 in 3D diagrams where the x-axis shows the amount of elements in the x direction, the y-axis
249 corresponds to the time in model time-steps (here one step corresponds to 20 years) and the z-
250 axis shows the non-dimensional height of the stylolite. The parameters for the two stylolites
251 shown in figure 5a and 5b are the same except for the absolute length (and height
252 respectively). The stylolite shown in figure 5a has an x-dimension of 0.4 cm whereas the
253 stylolite shown in figure 5b has an x-dimension of 40 cm.

254 The differences in absolute initial system size L have an effect on the dominance of
255 elastic versus surface energies during the roughening process. Surface energies become
256 increasingly more important towards smaller scales. This means that the stylolite in figure 5a,
257 which is relatively small ($L = 0.4$ cm) with a small grain size of $10\ \mu\text{m}$, is dominated by
258 surface energies so that elastic energies only play a minor role. The stylolite shown in figure
259 5b however is relatively large ($L = 40$ cm) with a large grain size of $1\ \text{mm}$ so that the elastic
260 energy dominates the roughening process and surface energies only play a minor role.

261 When comparing figures 5a and b (note that the z-axis scales differently, one unit
262 corresponds to 0.4 cm in a) and to 40 cm in b)), one observes that the roughness forms better
263 developed teeth with steep sides in the case of the larger stylolite (fig. 5b). The roughness of
264 the smaller stylolite (fig. 5a) is not growing smoothly but is disrupted quite often and
265 produces neither large amplitude nor well-developed teeth. In addition, the larger stylolite
266 (Fig. 5b) grows progressively while the small stylolite (Fig. 5a) shows an initial increase in
267 roughness that is followed by strong fluctuations in time, where the average roughness
268 amplitude remains more or less constant. These roughness evolutions imply that pinning
269 elements are destroyed when surface energy is high because of very high curvatures of spikes.
270 The interface of the surface energy dominated stylolite therefore contains no larger spikes or
271 teeth and is quite dynamic. Elastic energy on the other hand does not destroy spikes easily.
272 Therefore well-developed teeth structures tend to arise in larger stylolites at the outcrop scale
273 when surface energy is relatively unimportant, whereas we would expect to find less well-
274 developed teeth but rounder structures on the scale of a thin-section, where surface energy is
275 important.

276 In order to explore the evolution of the roughness amplitude with time, we use signal-
277 processing tools from statistical physics [26], as illustrated in the next section.

278 *3.3 Growth of the roughness with time*

279 The dynamics of a surface roughening process can be described by some basic scaling
 280 laws that are the same or at least very similar for different interfaces and surfaces (as e.g., gas-
 281 fluid interface motion in non-saturated porous media, propagation of flame fronts, atomic
 282 deposition processes, bacterial growth, erosion or dissolution fronts, contact line motion
 283 biphasic fronts over disordered pinning substrates, interfacial crack fronts). These laws,
 284 discovered by statistical physicists, describe how the amplitude of the roughness grows non-
 285 linearly with time, following power laws [26-29].

286 First we have to define an average value for the amplitude of the roughness of our
 287 numerical stylolites for each time step. We use the root mean square method to determine the
 288 average width of the stylolite roughness following [26]

$$289 \quad w(L,t) \equiv \sqrt{\frac{1}{L} \sum_{i=1}^L [h(i,t) - \bar{h}(t)]^2}, \quad (10)$$

290 where w is the interface width as a function of system size L and time t , h is the height of
 291 point i on the interface at time t and \bar{h} the average height of the interface at time t . This
 292 function gives an average width of the interface for each time step t and therefore
 293 characterizes the growth of the roughness. In our simulations, the system size L is defined as
 294 the number of elements in the x-direction. We use model sizes of 200 and 400 elements in the
 295 x-direction. The average height of the interface is defined as

$$296 \quad \bar{h}(t) \equiv \frac{1}{L} \sum_{i=1}^L h(i,t). \quad (11)$$

297 Statistical physics scaling laws [26] have demonstrated that, in many stochastic
 298 interfacial systems, roughening interfaces grow following a power law in time with a so-
 299 called growth exponent β . This is described by

$$300 \quad w(L,t) \sim t^\beta, \quad (12)$$

301 where the interface width w is proportional to time t to the power β , for a given system size L .
 302 If $\beta=1.0$, the interface grows linearly with time, if β is smaller than 1.0 the interface growth

303 slows down with time. Normal diffusion processes are characterized by $\beta=1/2$, anomalous
304 diffusion processes by $\beta \neq 1/2$, and $0 \leq \beta \leq 1$. In addition, for most stochastic interfacial
305 systems the width of roughening interfaces saturates after a critical time t_{crit} . This time
306 increases with the system size L .

307 When modelling the growth of stylolites, one can expect two scaling regimes in time,
308 first a power law up to time t_{crit} followed by a regime where w remains constant (Fig. 6a). In
309 order to study the dynamics of the roughening process one constructs diagrams of $\log_{10}(w)$
310 against $\log_{10}(t)$. The increase in width of the interface roughness should follow a straight line
311 where the slope of the line gives the growth exponent β . After a critical time t_{crit} the
312 roughness saturates and the slope vanishes to zero (Fig. 6a).

313 We studied three simulations (Fig. 6b-d) with this method, where the simulation
314 shown in figure 6b has a system size $L = 0.4$ cm, the simulation shown in figure 6c has $L = 4$
315 cm and the one shown in figure 6d has $L = 40$ cm. Figure 6b and 5a and figure 6d and 5b
316 show the same simulations, respectively. The simulated stylolite shown in figure 6b shows the
317 expected behaviour with two scaling regimes, the roughness first grows with a roughness
318 exponent of 0.5 and saturates after 2500 years, where it remains constant close to a value of
319 50 μm . Going back to figure 5a where the growth of the same stylolite is illustrated in 3d, the
320 roughness saturates after 2500 years, which corresponds to model time step 125. Figures 6c
321 and d show only the first scaling regime where the increase in roughness amplitude w follows
322 a power law, but w never saturate. That means probably that these two simulations (Fig. 6c, d)
323 did not reach the critical time needed for the roughness to saturate. Taking a look at figure 5b
324 where the growing roughness of the stylolite shown in figure 6d is illustrated, the roughness
325 width still grows i.e. is not yet saturated.

326 The three stylolites shown in figure 6b-d seem to have different critical times when the
327 roughness saturates but also their growth exponents vary. β increases from the smallest
328 simulation (fig. 6b) with a value of 0.5 through the medium-sized simulation with a value of

329 0.54 to the largest simulation with a value of 0.8. These differences may reflect differences of
 330 growth regimes that are dominated by either surface energy or by elastic energy, in analogy to
 331 the discussion on figures 5a and b. The surface energy dominated growth regime (small
 332 stylolite, fig. 6b) has a growth exponent of 0.5 and saturates relatively early. The stylolite
 333 shown in figure 6c is intermediate, the growth exponent is still small with 0.54 but the
 334 roughness does not saturate within the simulated time. The largest stylolite (fig. 6d) has a
 335 significantly larger growth exponent of 0.8, does not saturate, and represents the elastic
 336 energy dominated regime.

337 In terms of natural stylolites the above-mentioned values demonstrate that small
 338 stylolites that grow within the surface energy dominated regime grow as slow as a diffusive
 339 process (exponent of 0.5) and saturate early so that compaction estimates are almost
 340 impossible. However, stylolites that grow within the elastic energy dominated regime grow
 341 faster (exponent 0.8) and do not seem to saturate after 8000 years. They can thus capture part
 342 of the compaction of the rock even though their growth is non-linear, and slows down with
 343 time. Consequently, rather than using a rule of thumb as a direct proportionality between A ,
 344 the amplitude of compaction displacement accommodated for around a stylolite, and the
 345 stylolite amplitude w , the nonlinear power-law observed for this process where the imposed
 346 displacement is linear in time can be utilized to be stated as $(w/l) \sim (t/t_0)^\beta \sim (A/D)^\beta$, with
 347 l the relevant physical length, which is here the grain size.

348 Conversely, for large enough stylolites, as long as the critical saturation time has not
 349 been reached at the observed scale, the relationship between the total compaction
 350 displacement A and the stylolite amplitude should be of the type

$$351 \quad A \sim (w/l)^{1/\beta} l. \quad (13)$$

352 This law should hold until the critical saturation time is reached. Using the proposed scaling
 353 law for the large simulation ($L = 40\text{cm}$) we obtain the right relation with a slope of 6.6 (Fig.
 354 7) using the root mean square width and a grain size of 1mm. The stylolite amplitude may

355 finally saturate, but this seems not to happen in 8000 years for the case of the 40 cm long
356 stylolites that we have studied.

357 *3.4 The teeth structures and their relation with the main compressive stress direction*

358 After characterizing the dynamics of the growth process, we now focus on the
359 orientation of the stylolite teeth. We have demonstrated so far that the teeth mainly develop in
360 the regime where elastic energy is dominant so that well-developed teeth form in the stylolite
361 simulation with a system size $L = 40\text{cm}$. The steep sides of the teeth are thought to develop
362 parallel to the main compressive stress and the top of the teeth is thought to be oriented
363 perpendicularly to that stress direction.

364 We test this hypothesis that the teeth track the orientation of the largest principal
365 stress. For the test, we choose again a model with an initially flat dissolution surface that is
366 oriented horizontally with respect to the simulation box but we rotate the compression
367 direction so that the stress field rotates. Theoretically, the teeth should follow the rotated
368 stress field so that one can evaluate the direction of the main compressive stress using the
369 teeth orientation. We use simulations with a system size of 200 elements in the x-direction
370 with an absolute size of $L = 10\text{ cm}$ so that we are in the elastic regime.

371 The results of the 5 different simulations are shown in figure 8 a-e where the
372 orientation of the compression direction is shown on the left hand side. Indeed, the teeth do
373 follow the stress directions in all the examples. The sides of the teeth are the best stress
374 direction indicators but even the tops of some teeth tend to orient themselves with respect to
375 the stress. The most extreme example is shown in figure 8e where the compression direction
376 has a very low angle with respect to the initial horizontal heterogeneity. The initially
377 horizontal surface has vanished and a stair-step geometry develops with steps that are oriented
378 perpendicular with respect to each other. One set of surfaces corresponds to the sides of the
379 teeth and the other set to the top surface of the teeth.

380 These simulations demonstrate that stylolite teeth indeed track the direction of the
381 main compressive stress and can therefore be used as stress indicators in natural rocks.

382 *3.5 Model for the deterministic orientation of stylolite teeth*

383 Our simulations have shown that well-developed stylolite teeth only tend to develop in
384 the elastic regime (Fig. 5). In order to understand the relation between the compaction
385 direction and the orientation of the stylolite teeth, we consider the stress distribution at the
386 interface and the finite compaction. The stress field at the interface for a given time step is
387 directly controlling dissolution. However, just observing the stress field across a stylolite for a
388 single time step is not enough since dissolution and thus a change in the geometry of the
389 interface influences the stress back, dissolution and stress being highly coupled. Therefore we
390 also have to consider the whole stress history and the finite compaction across the interface.

391 Going back to figure 4, one can observe that the location of the teeth is random
392 because it depends on the quenched noise in the background. The second simple observation
393 is that the finite compaction is directly recorded by the pinning of particles (Fig. 4). As long
394 as they pin the interface, they move in the direction of the compaction, which is parallel to the
395 far field compressive stress for a simple homogeneous rock. This scenario does not change
396 when the compaction direction and thus the main compressive stress is not perpendicular to
397 the initial interface (Fig. 9a). Pinning particles still record the rotated compaction direction
398 because they move in that direction. If two pinning elements are close but on opposing sides
399 of the interface they move in opposite directions and a perfect side of a tooth develops
400 recording the compaction direction. If this direction is parallel to the far field main
401 compressive stress, the stylolite also records this stress direction.

402 Looking at the movement of a whole interface (Fig. 9b), one can see that the total amount that
403 the interface may move perpendicularly to itself depends on its orientation with respect to the
404 compaction direction. An interface that is oriented perpendicularly to the compaction
405 direction can have the largest fluctuations and thus produce a roughness with the largest

406 amplitude. An interface that is oriented at a smaller angle to the compaction direction will not
407 develop importantly in the direction perpendicular to itself. If particles are pinning this
408 interface, it may actually develop steps. The most extreme case is an interface that is oriented
409 parallel to the compaction direction. This interface shows no fluctuations and thus cannot
410 develop a roughness. It cannot even develop steps because particles cannot pin this interface.
411 The interface is very stable and can only act as a transform fault. Therefore the sides of teeth,
412 which reflect such an interface, are very stable and the teeth geometry itself is a natural
413 consequence of the compaction direction (Fig. 9c). Strongly pinning particles are not even
414 necessary for the development of these geometries. Some pinning or a variation in dissolution
415 across the interface is necessary for a roughening of the interface, but once this roughness is
416 initiated and for large scales where the surface energy is not dominant, the typical teeth
417 geometries develop and stay stable without much flickering, i.e. they are strongly
418 deterministic.

419 Looking at the stress history, we also show that the main compressive stress close to
420 the stylolite is parallel to the main compaction direction. An interface perpendicular to the
421 main compaction direction has a significantly normal stress component and experiences
422 dissolution. For an interface parallel to the main compressive stress, dissolution will only
423 relax the second principle stress that builds up in a laterally confined system. The second
424 principle stress will vanish to zero and in the extreme case a hole can develop. Compaction
425 itself cannot fill the hole because the compaction has the wrong direction. The only possibility
426 to build-up stress again is a flow of material into the hole or a collapse of the teeth. Looking at
427 the stress history, the main compressive stress close to the stylolite and the direction of the
428 finite compaction are parallel. Indeed, the stylolite teeth track this direction.

429 **4. Discussion**

430 In this discussion we first focus on several assumptions used in the simulations. The
431 focus of these simulations is the roughening process of an initially smooth interface, not an

432 investigation of the reason why the dissolution is localized. Therefore we use an initially flat
433 interface where dissolution starts and restrict dissolution to this stylolite surface. Some
434 observations in natural rocks support such a scenario: First, some stylolites do initiate from
435 mica-rich layers. Next, some stylolites with oblique teeth do exist. Stylolites with oblique
436 teeth are most probably initiating from an interface that was oblique with respect to the main
437 compressive stress direction when the stylolite roughness started to grow. However, surely
438 not all stylolites start from given heterogeneities but may localize due to geochemical self-
439 organization [30] or anti-cracking [16]. This is beyond the focus of this current manuscript.

440 In our simulations, we use a simple description of the noise that initiates the
441 roughening process. As mentioned earlier, the noise is only chemical (a variation in
442 dissolution constants), is set on single particles that have the same size and is distributed with
443 a bimodal distribution. In a real rock, elastic properties and surface energy may also vary, the
444 noise may be on the grain scale or at the scale of smaller heterogeneities and the distribution
445 may be more complicated than bimodal. It is not clear how variations in these parameters may
446 affect the stylolite growth and what kind of noise is present in a real rock. The nature of the
447 noise may influence pinning of the surface and thus may influence the growth and structure of
448 the stylolite [31]. However, since our simulations can reproduce natural stylolites quite
449 realistically, one can argue that the exact nature of the noise is less important than the effects
450 of elastic energy, surface energy and stress.

451 Another interesting question is how a stylolite grows when the finite strain is rotating.
452 We have demonstrated that stylolite teeth develop by a particle pinning process at the
453 interface and track the direction of the finite compaction. However, this is not necessarily true
454 if the finite strain is rotating because particles at the interface only pin the interface from the
455 moment when they meet the interface to the moment when they dissolve. This means that
456 they are only recording parts of the finite compaction direction. If the stylolite grows in a
457 simple shear dominated rock, the direction of the pinning particles should initially record the

458 direction of the compressive ISA (incremental stretching axes) and then the teeth should
459 rotate. Therefore young teeth do really track the compressive ISA and thus probably also the
460 direction of the compressive stress whereas old teeth rotate. However, if the roughness is
461 dynamic and the stylolite constantly changes its shape, it can always grow new teeth and old
462 teeth will disappear so that the direction of the compressive ISA and the compressive stress
463 are recorded.

464 **5. Conclusions**

465 We have developed a numerical model that can successfully reproduce the roughening
466 of stylolites. The numerical stylolites are very similar, if not identical, to natural stylolites. We
467 propose that the growth of the stylolite roughness is induced by pinning particles, that
468 produce a complex interface that evolves dynamically through time. Two different regimes
469 can be separated, a small-scale regime where the roughness fluctuates significantly and a
470 large-scale regime where well-developed teeth patterns grow. The small-scale regime is
471 dominated by surface energy whereas the large-scale regime is dominated by elastic energy.
472 Scaling laws characterizing the dynamic growth of the stylolite roughness as a function of
473 time are proposed. These laws show that the roughness grows in two successive regimes in
474 time, a first regime where the growth follows a power law and a second regime where the
475 roughness growth saturates. These findings are essential for compaction estimates using
476 stylolites, the roughness growth is non-linear in time, slows down with time and may even
477 saturate. A saturated stylolite loses its memory for compaction completely and cannot be
478 used for total compaction or strain rate estimates. We also show with our simulations that the
479 teeth of stylolites do really follow the main compaction direction and may thus indicate the
480 direction of the maximum compressive stress in a homogeneous rock. We show that this
481 strong deterministic geometry of the teeth is a consequence of pinning particles that move in
482 the direction of the finite compaction and of the local stress history at the stylolite interface.
483 Summarizing, the geometry of stylolite teeth can be used by geologists to estimate the

484 direction of the finite compaction or the main compressive stress, but absolute compaction
485 estimates are difficult to perform and may strongly underestimate the real values. In the
486 regime preceding saturation, we utilize the observed nonlinear growth of the roughness
487 amplitude to propose a refined estimate of absolute compaction, Eq. (13), based both on the
488 stylolite roughness amplitude and the size of the dissolving grains (Fig. 7). This can in general
489 be used as a lower bound of total compaction.

490

491 **Acknowledgements:**

492 DK acknowledges funding by the MWFZ Center of Mainz University and the DFG (KO
493 2114/5-1). This is contribution No. 37 from the Geocycles Cluster funded by the state of
494 Rheinland-Pfalz.

495

496 **References**

- 497 [1] P.B. Stockdale, Stylolites: their nature and origin. *Indiana University Studies IX*, (1922) 1-
498 97.
- 499 [2] M.T. Heald, Stylolites in sandstones. *The Journal of Geology*. 63, (1955) 101-114.
- 500 [3] W. Park, E. Schot, Stylolites: their nature and origin, *J. Sedimen. Petrol.*, 38, (1968) 175-
501 191.
- 502 [4] R. Bathurst, *Carbonate sediments and their diagenesis*, Elsevier Sci. New York, (1971).
- 503 [5] B. Bayly, A mechanism for the development of stylolites, *Journal of Geology*, 94, (1986)
504 431-435.
- 505 [6] F. Renard, J. Schmittbuhl, J.-P. Gratier, P. Meakin, E. Merino, Three-dimensional
506 roughness of stylolites in limestones, *J. Geophys. Res.*, 108, (2004) B03209.
- 507 [7] Z. Karcz, C.H. Scholz, The fractal geometry of some stylolites from the Calcare Massiccio
508 Formation, Italy. *Journal of Structural Geology*, 25, (2003) 1301-1316.

- 509 [8] J. Schmittbuhl, F. Renard, J.-P. Gratier, R. Toussaint, The roughness of stylolites:
510 Implications of 3D high resolution topography measurements, *Phys. Rev. Lett.*, 93, (2004)
511 238501.
- 512 [9] J. Suppe, *Principles of Structural Geology*, Prentice-Hall, New Jersey, (1985) 537.
- 513 [10] H. Stel, M.J. De Ruig, Opposite vergence of a kink fold and pressure solution cleavage,
514 southeast Spain: a study of the relation between paleostress and fold kinematics.
515 *Tectonophysics* 165, (1989) 117-124.
- 516 [11] J.-P. Petit, M. Mattauer, Paleostress superimposition deduced from mesoscale structures
517 in limestone: the Matelles exposure, Languedoc, France. *Journal of Structural Geology* 17,
518 (1995) 245-256.
- 519 [12] M. Ebner, B. Grasemann, Divergent and convergent non-isochoric deformation. *Journal*
520 *of Structural Geology*, 28, (2006)1725-1733.
- 521 [13] D.C.P. Peacock, I.N. Azzam, Development and scaling relationships of a stylolite
522 population. *Journal of Structural Geology*, 28, (2006) 1883-1889.
- 523 [14] J. Gratier, L. Muquet, R. Hassani, F. Renard, Experimental microstylolites in quartz and
524 modeled application to natural stylolitic structures, *Journal of Structural Geology*, 27,
525 (2005) 89-100.
- 526 [15] C.N. Drummond, D.N. Sexton, Fractal structure of stylolites, *Journal of Sedimentary*
527 *Research*, 68, (1998) 8-10.
- 528 [16] R.A. Fletcher, D.D. Pollard, Anticrack model for pressure solution surfaces. *Geology* 9,
529 (1981) 419-424.
- 530 [17] R. Katsman, E. Aharonov, H. Scher, Localized compaction in rocks: Eshelby's inclusion
531 and the spring network model. *Geophysical Research Letters*, 33, (2006) L10311
- 532 [18] M.W. Jessell, P.D. Bons, L. Evans, T.D. Barr, K. Stüwe, Elle, The numerical simulation
533 of metamorphic and deformation textures. *Computers and Geosciences*, 27, (2001) 17-30.

- 534 [19] D. Koehn, J. Arnold, A. Malthe-Sørenssen, B. Jamtveit, Instabilities in stress corrosion
535 and the transition to brittle failure, *American Journal of Science*, 303, (2003) 956-971.
- 536 [20] D. Koehn, A. Malthe-Sørenssen, C. Passchier, The structure of reactive grain-boundaries
537 under stress containing confined fluids. *Chemical Geology*, 230, (2006) 207-219.
- 538 [21] S. McNamara, E.G. Flekkoy, K.J. Maløy, Grains and gas flow: Molecular dynamics with
539 hydrodynamic interactions. *Phys. Rev. E* 61, (2000) 4054-4059.
- 540 [22] O. Johnsen, R. Toussaint, K.J. Maløy, E.G. Flekkøy, Pattern formation during air
541 injection into granular materials confined in a circular Hele-Shaw cell. *Phys. Rev. E*, 74,
542 (2006) 011301.
- 543 [23] L.D. Landau, E.M. Lifshitz, *Theory of Elasticity*. New York, Pergamon Press, (1959)
544 134.
- 545 [24] E.G. Flekkøy, A. Malthe-Sørenssen, B. Jamtveit, Modeling hydrofracture. *Journal of*
546 *Geophysical research* B8, 107, ECV 1, (2002) 1-11.
- 547 [25] M.S. Paterson, *Nonhydrostatic thermodynamics and its geologic applications*. *Reviews*
548 *of Geophysics Space Physics*, 11, (1973) 355-389.
- 549 [26] A. L. Barabási, E.H. Stanley E. H., *Fractal concepts in surface growth*, Cambridge Univ
550 Press. New York (1995).
- 551 [27] F. Family, T. Vicsek, *Dynamics of fractal surfaces*. World Scientific Publishing,
552 Singapore New Jersey London Hong Kong (1991).
- 553 [28] S. Moulinet, A. Rosso, W. Krauth, E. Rolley, Width distribution of contact lines on a
554 disordered substrate, *Phys. Rev. E*, 69, (2004) 035103(R).
- 555 [29] K.J. Maløy, S. Santucci, J. Schmittbuhl, R. Toussaint, Local waiting time fluctuations
556 along a randomly pinned crack front. *Phys. Rev. Lett.*, 96, (2006) 045501.
- 557 [30] T. Dewers, P. Ortoleva, A coupled reaction/transport/mechanical model for intergranular
558 pressure solution, stylolites, and differential compaction and cementation in clean
559 sandstones. *Geochimica et Cosmochimica Acta*, 54, (1990) 1609-1625.

560 [31] A. Brouste, F. Renard, J.-P. Gratier, J. Schmittbuhl, Variety of stylolite morphologies
561 and statistical characterization of the amount of heterogeneities in the rock, Journal of
562 Structural Geology, in press (2007).

563 **Figure captions**

564 Figure 1. Natural stylolites on a limestone quarry surface from the Burgundy area, France. On
565 the large scale the stylolites are planar structures whereas on the small scale they show a
566 pronounced roughness (see inset). Note the steep "teeth" like patterns in the inset.

567

568 Figure 2. a) weight function used in the coarse graining procedure to evaluate the surface
569 energy. b) setup of the numerical model. Side-walls are fixed whereas the upper and lower
570 walls are moved inwards to compact the system. The rock contains two kinds of particles that
571 dissolve at two different rates. This heterogeneity in the dissolution rate represents an initial
572 quenched noise in the rock.

573

574 Figure 3. Simulated stylolite with a width of $L = 40$ cm (1:1). Note similarities between the
575 natural stylolite (in Figure 1) and the simulated stylolite. Both develop a roughness on
576 different scales and well-developed square teeth structures.

577

578 Figure 4. Particles pinning along the interface. (a) Initial setup of a simulation with the initial
579 interface in the centre and the quenched noise in the background (particles that dissolve twice
580 slower are dark). (b)-(d) Progressive growth of the roughness and pinning of the interface
581 (particles that pin are white). (e) Structures that develop during pinning: spikes, teeth that are
582 pinned in one direction and teeth that are pinned in two directions.

583

584 Figure 5. 3D diagrams showing the growth of two stylolites. (a) Small stylolite that grows in
585 the surface energy dominated regime (x dimension is $L = 0.4$ cm). The growth of the
586 roughness slows down relatively fast and saturates. The growth is very dynamic so that
587 pinning particles are dissolved relatively fast. (b) Large stylolite that grows in the elastic

588 energy dominated regime (x dimension is $L = 40$ cm). The stylolite roughness grows
589 continuously and develops well-developed teeth.

590

591 Figure 6. Log/log diagrams showing the growth of the roughness amplitude w (one unit =
592 0.004 m) against time (t , model steps). (a) Schematic diagram illustrating the two regimes that
593 should develop [26]. Regime I shows a growth that follows a power law in time with a growth
594 exponent β until a critical time. Regime II is characterized by a saturation of the growth so
595 that the roughness amplitude remains constant. (b) Small stylolite ($L = 0.4$ cm) that shows both
596 regimes, a power law growth with an exponent of 0.5 in regime I (as slow as a diffusive
597 process) and a crossover regime II where the roughness saturates. (c) Medium sized stylolite
598 ($L = 4$ cm) that shows only the regime I with a power law growth with an exponent of 0.54.
599 (d) Large stylolite ($L = 40$ cm) that shows only regime I with a power law growth with an
600 exponent of 0.8.

601

602 Figure 7. Proposed scaling relation between the amplitude of compaction around a stylolite
603 (A) and the mean width of the stylolite roughness (w). l corresponds to the grain size and β is
604 the predetermined growth exponent (0.8 in this case). Plot shows the scaling relation for the
605 large stylolite simulation (40cm long stylolite) using equation 13. Theoretically this scaling
606 relation with the determined prefactor of 6.6 can be used to estimate compaction from real
607 stylolites.

608

609 Figure 8. Stylolite teeth directions track variations of the compression direction. The
610 orientation of the initial interface is given at the top and the direction of the compaction is
611 illustrated at the left hand side. The simulations show that the orientation of the teeth is
612 strongly deterministic and follows the compaction direction.

613

614 Figure 9. Model for the development of stylolite teeth. (a) Development of oblique teeth due
615 to pinning particles that record the relative movement of the rock on each side of the interface.
616 (b) Possible fluctuations that may develop on interfaces with different orientations with
617 respect to the main compaction direction. Strongest fluctuations appear on interfaces that are
618 oriented perpendicular with respect to the main compaction direction (arrows). Interfaces that
619 are parallel to the main compaction direction do not show fluctuations. (c) Illustration of these
620 fluctuations on a natural stylolite. The sides of teeth are relatively stable, show no fluctuations
621 and may act as transform faults. Plateaus of teeth are interfaces that show largest fluctuations.

Figure
[Click here to download high resolution image](#)



Fig. 1

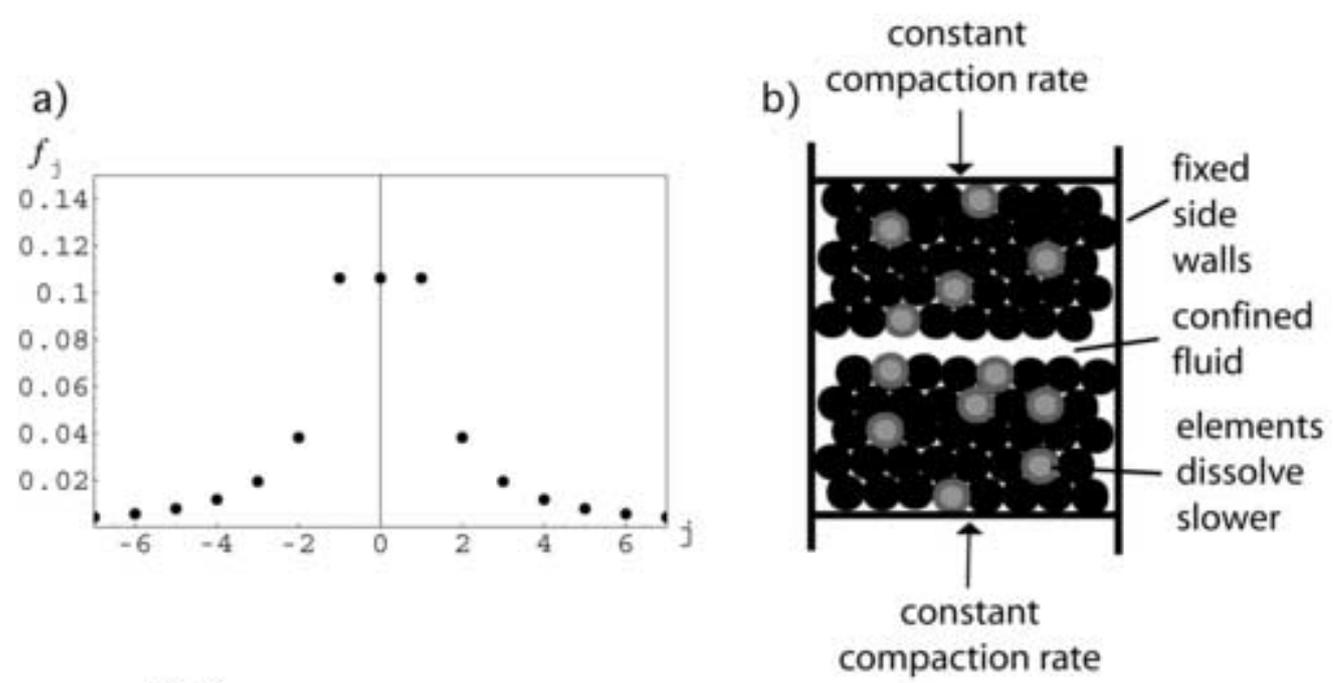


Fig.2

Figure
[Click here to download high resolution image](#)

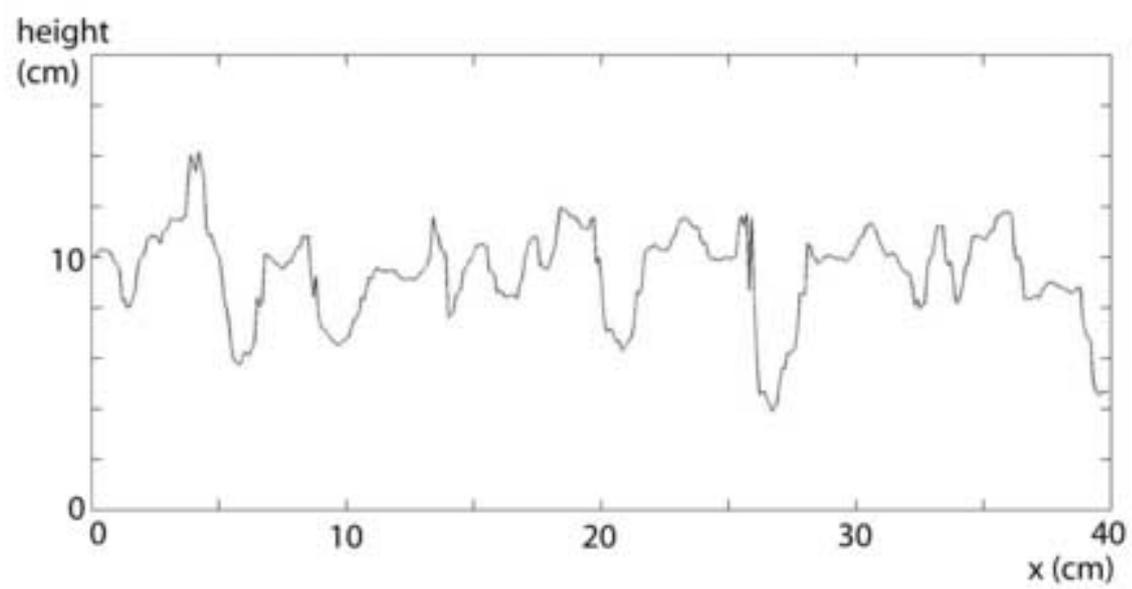


Fig.3

Figure
[Click here to download high resolution image](#)

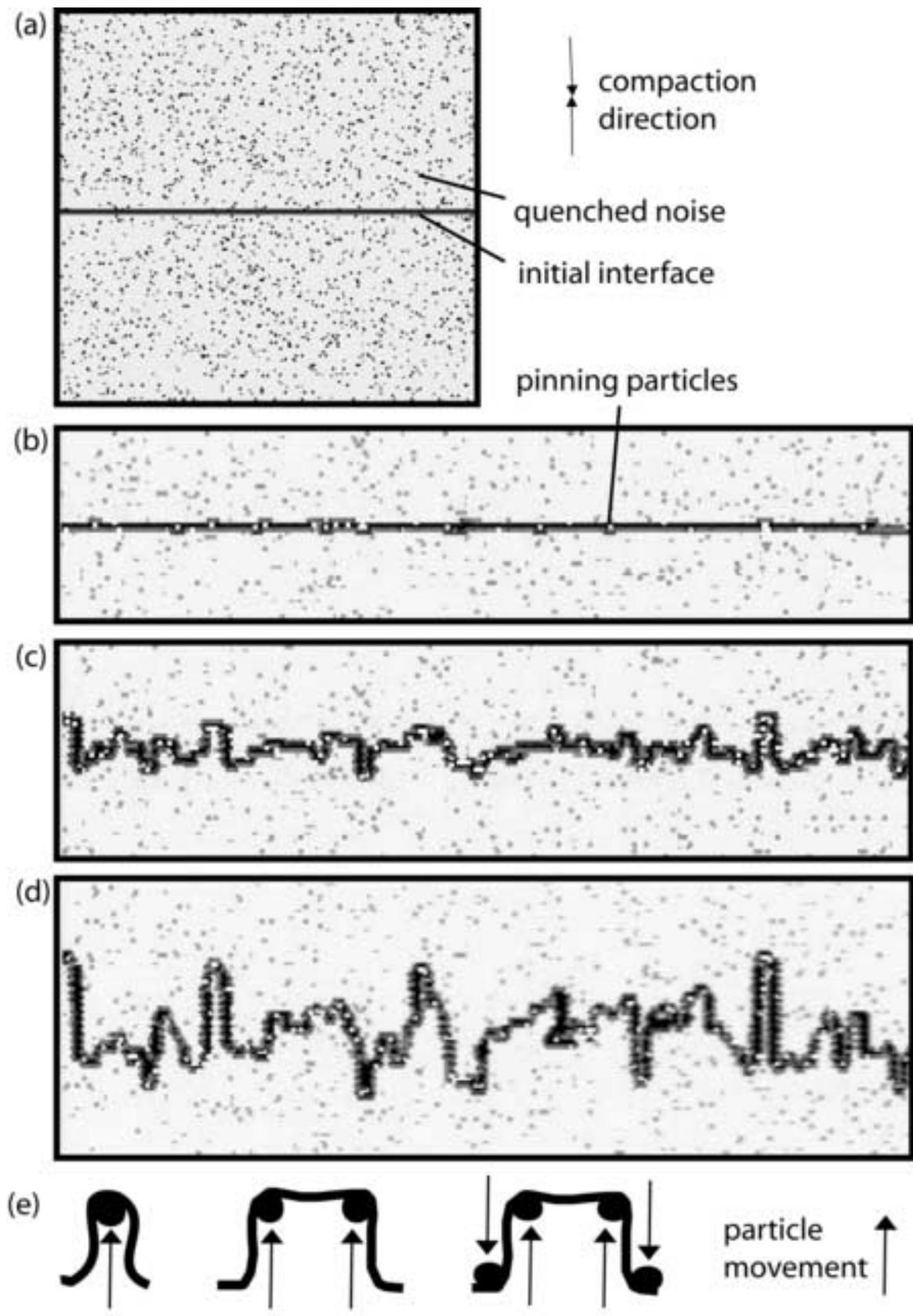


Fig. 4

Figure
[Click here to download high resolution image](#)

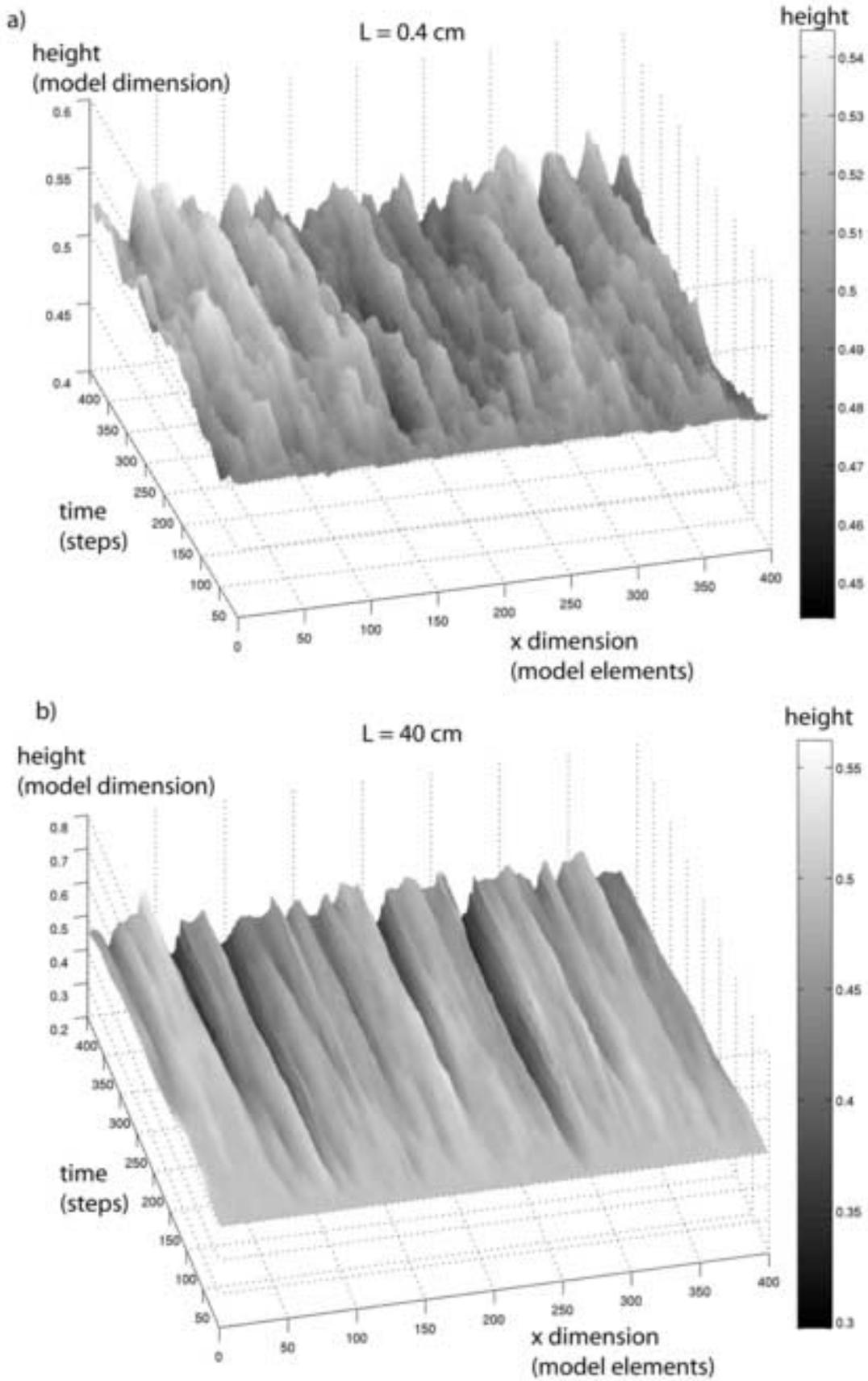


Fig. 5

Figure
[Click here to download high resolution image](#)

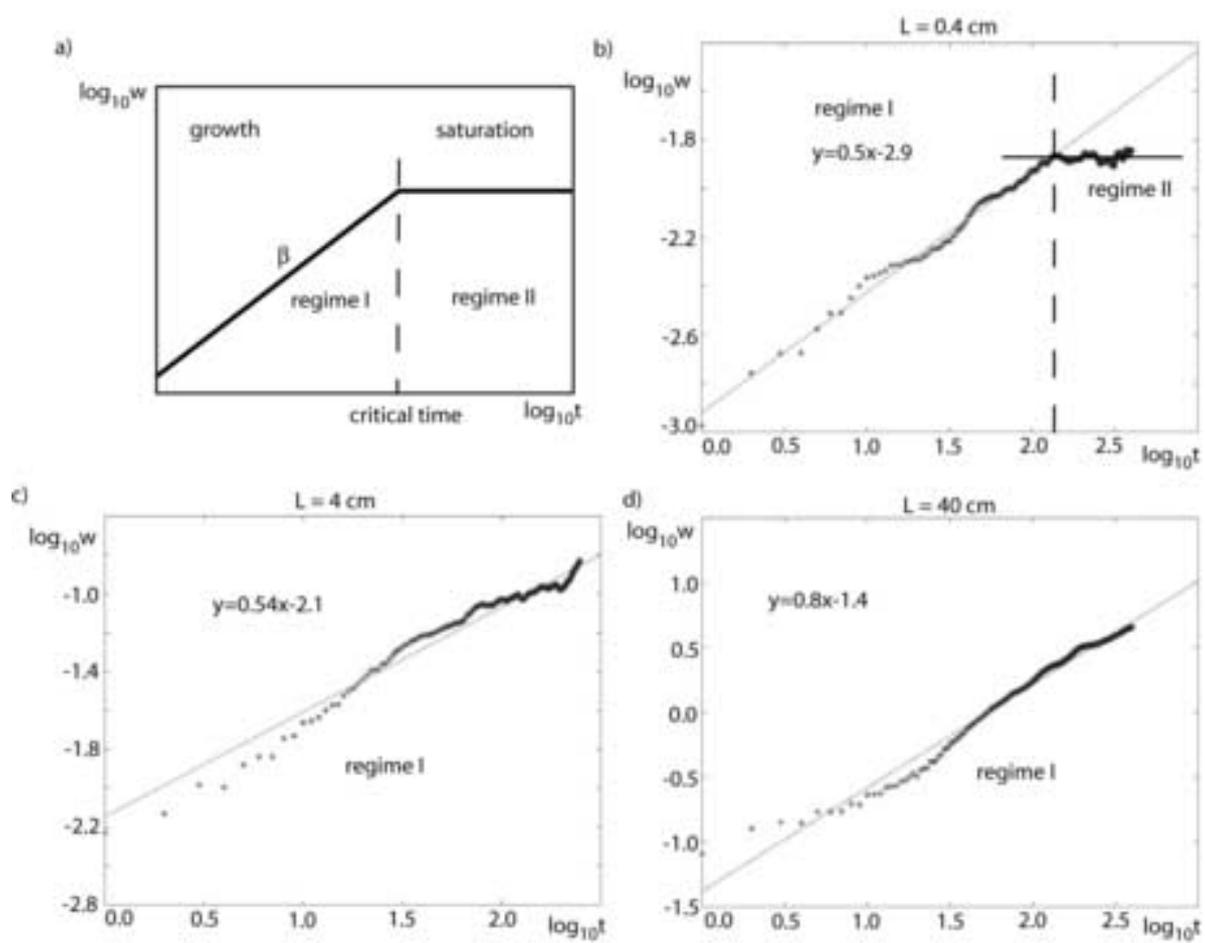


Fig. 6

Figure
[Click here to download high resolution image](#)

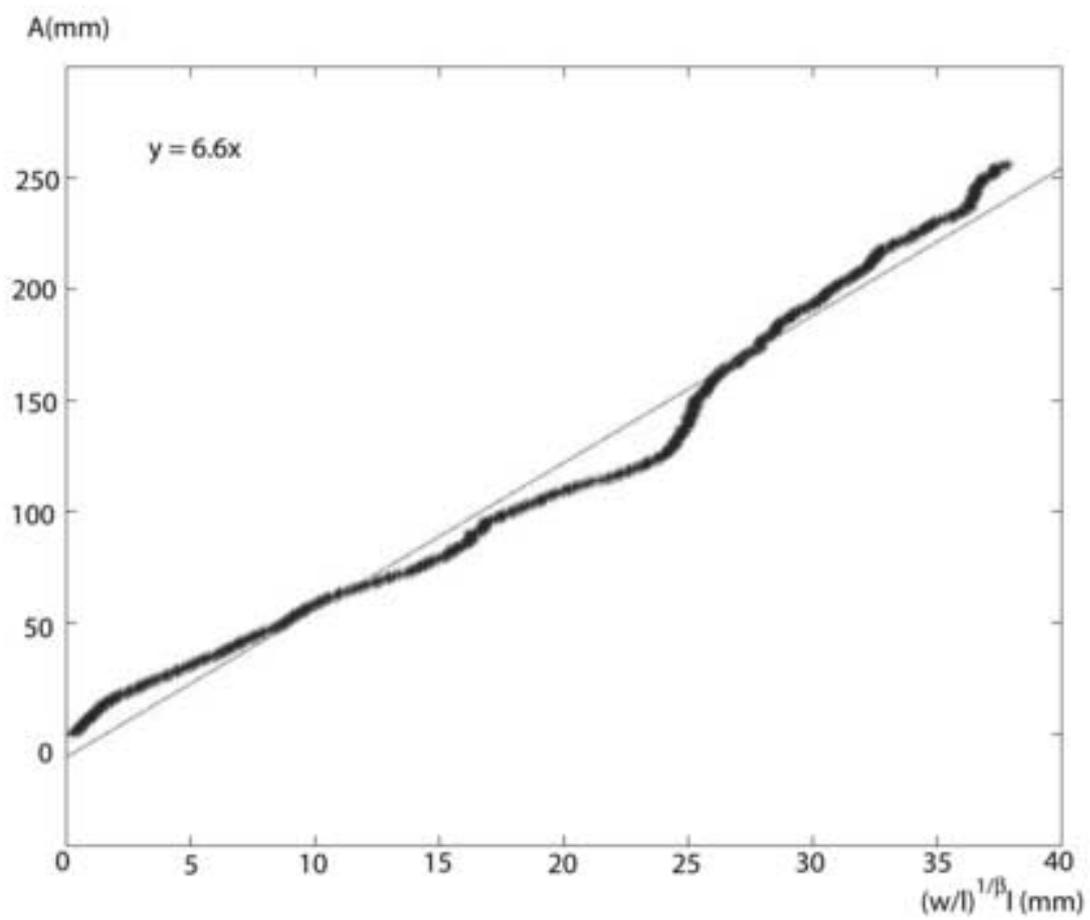


Fig. 7

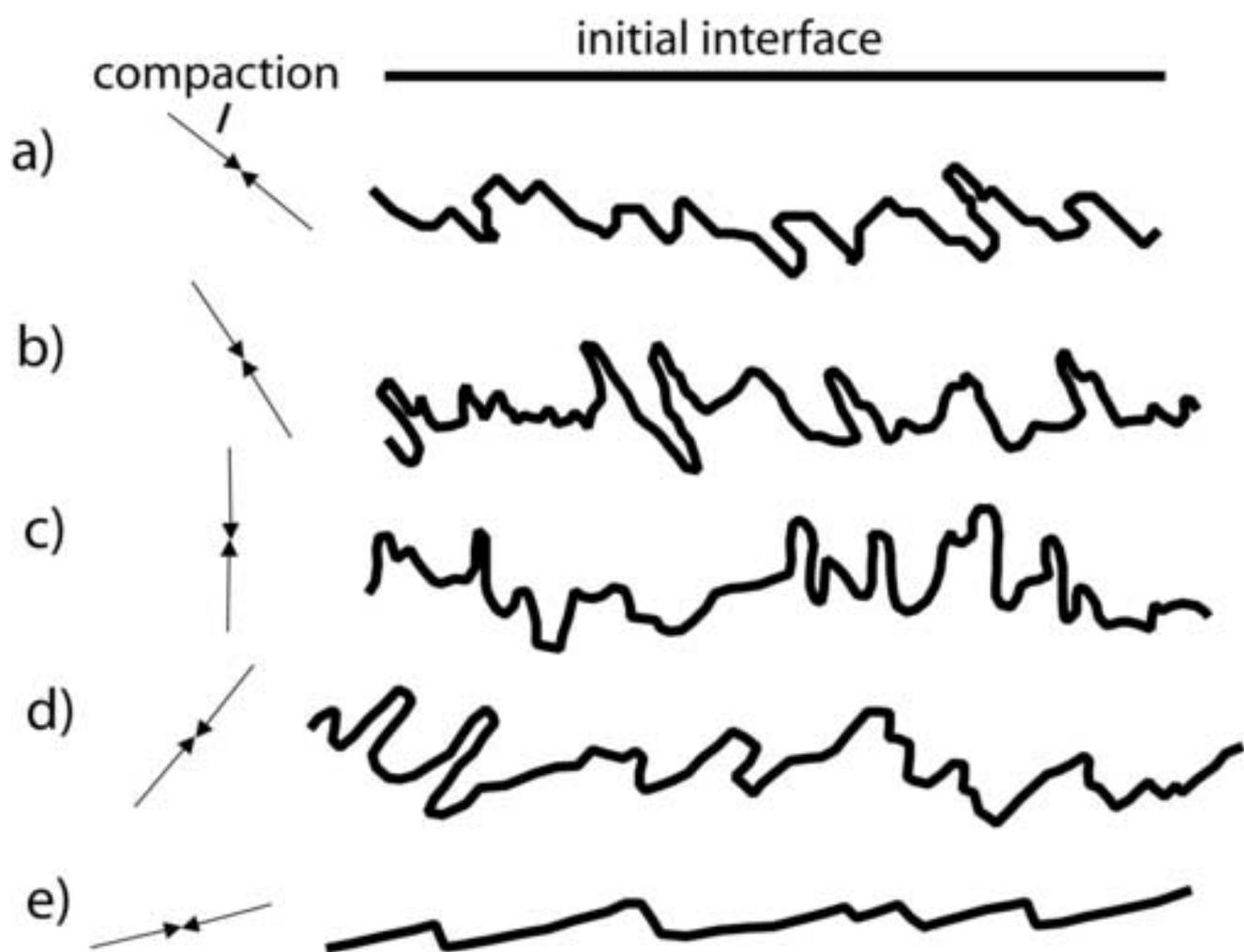


Fig. 8

Figure
[Click here to download high resolution image](#)

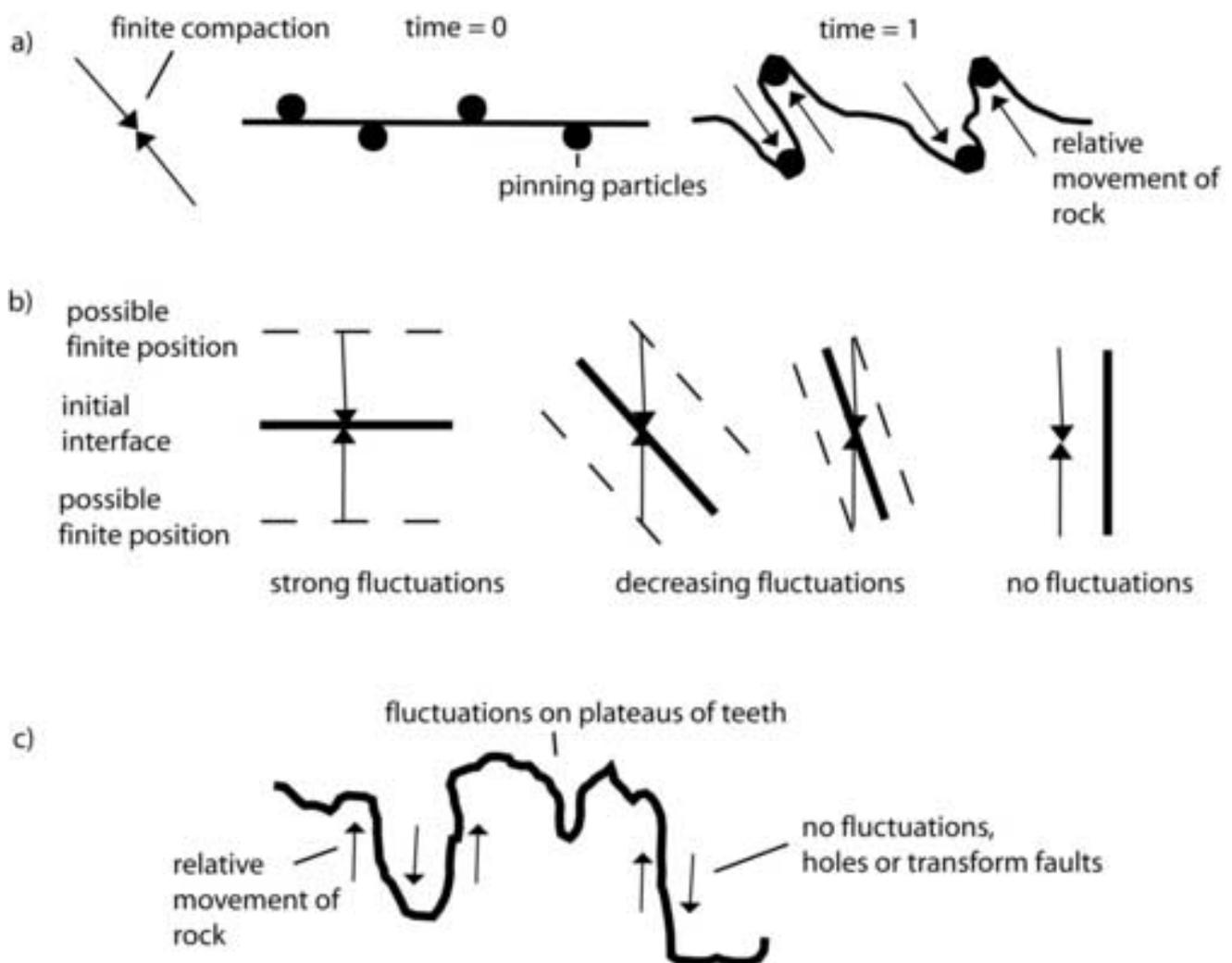


Fig.9